Thermal and structural stability of Zr–based amorphous thin films for potential application in hydrogen purification

Nayebossadri, Shahrouz; Greenwood, Carmel; Speight, John; Book, David

DOI:
10.1016/j.seppur.2017.06.052

Document Version
Peer reviewed version

Citation for published version (Harvard):
Nayebossadri, S, Greenwood, C, Speight, J & Book, D 2017, 'Thermal and structural stability of Zr–based amorphous thin films for potential application in hydrogen purification', *Separation and Purification Technology*, vol. 187, pp. 173-183. https://doi.org/10.1016/j.seppur.2017.06.052

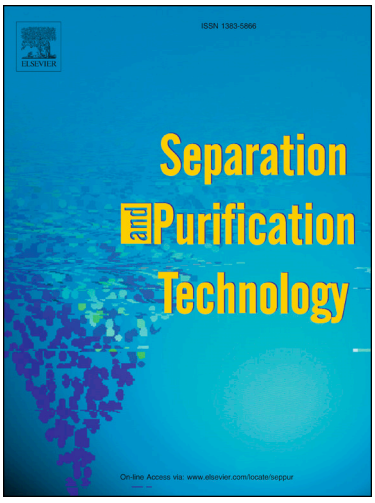

Thermal and structural stability of Zr–based amorphous thin films for potential application in hydrogen purification

Shahrouz Nayebossadri, Carmel J. Greenwood, John D. Speight, David Book

PII: S1383-5866(17)30419-7
DOI: http://dx.doi.org/10.1016/j.seppur.2017.06.052
Reference: SEPPUR 13830

To appear in: *Separation and Purification Technology*

Received Date: 6 February 2017
Revised Date: 19 June 2017
Accepted Date: 19 June 2017

Please cite this article as: S. Nayebossadri, C.J. Greenwood, J.D. Speight, D. Book, Thermal and structural stability of Zr–based amorphous thin films for potential application in hydrogen purification, *Separation and Purification Technology* (2017), doi: http://dx.doi.org/10.1016/j.seppur.2017.06.052

Thermal and Structural Stability of Zr–Based Amorphous Thin Films for Potential Application in Hydrogen Purification

Shahrouz Nayebossadri*, Carmel J. Greenwood, John D. Speight, David Book
School of Metallurgy and Materials, University of Birmingham,
Edgbaston, Birmingham, B15 2TT, UK
*E-mail: s.nayebossadri@bham.ac.uk
Tel: (+44) (0) 121 414 5213

Abstract

Amorphous alloys are of particular interest due to their less susceptibility to hydrogen embrittlement and corrosion, superior mechanical properties and more importantly lower cost compared to the Pd–based crystalline membranes. Amorphous thin films of $Zr_{40.5}Ni_{59.5}$, $Zr_{56.2}Cu_{43.8}$, $Zr_{30}Cu_{57.7}Y_{12.3}$, and $Zr_{32}Cu_{57.3}Ti_{10.7}$ alloys are fabricated by the magnetron sputtering method. All alloys are thermally stable until above 400 °C under an inert atmosphere. Nevertheless, the thermal stabilities of all alloys are reduced by almost more than 150 °C under hydrogen with exception of the $Zr_{40.5}Ni_{59.5}$ alloy showing comparable thermal stability under hydrogen and inert. Structural analyses by XRD under hydrogen and an inert atmosphere reveal decomposition of the studied amorphous alloys during the crystallisation process, leading to severe phase separation for Ni and Cu in $Zr_{40.5}Ni_{59.5}$ and $Zr_{56.2}Cu_{43.8}$ alloys. Such a phase separation seems to have an influence on the crystallisation path and products. However, Cu phase separation seems to be mitigated in $Zr_{30}Cu_{57.7}Y_{12.3}$, and $Zr_{32}Cu_{57.3}Ti_{10.7}$ alloys despite their higher Cu content compared to $Zr_{56.2}Cu_{43.8}$ alloy. The surface segregation tendency of Cu results in surface crystallisation in the $Zr_{56.2}Cu_{43.8}$ alloy, whilst bulk nucleation and growth dominates the crystallisation process in the other alloys, evident by the non–isothermal kinetic studies. The calculated activation energies show that more energy is required for nucleation compared to the growth process in the $Zr_{40.5}Ni_{59.5}$ and $Zr_{56.2}Cu_{43.8}$ alloys, whilst is the opposite case in $Zr_{30}Cu_{57.7}Y_{12.3}$, and $Zr_{32}Cu_{57.3}Ti_{10.7}$ alloys.

Keywords: *Thin film, Amorphous alloy, Magnetron sputtering, Zr–based alloys, Crystallisation, Hydrogen purification*

1-Introduction

The application of amorphous alloys for hydrogen separation is preferable over the conventional Pd–based crystalline membranes due to their good mechanical properties, increased resistance to hydrogen embrittlement and lower cost [1]. Amorphous materials also exhibit increased strength, ductility, corrosion resistance, and hydrogen solubility compared to crystalline materials [2]–[5]. Such desired properties have motivated numerous studies [1]–[3] to explore a variety of amorphous alloys for hydrogen separation. However, since amorphous membranes are thermodynamically metastable, their application is limited due to their crystallisation tendency, once isothermally kept close to (time dependent crystallisation) or heated above (temperature dependent crystallisation) the crystallisation temperature [2], [6], [7]. Hence, the development of amorphous alloys aims to identify thermally stable amorphous membranes with equal or higher hydrogen permeability than Pd.

$Zr_{36}Ni_{64}$ alloy showed [8] to be only permeable to hydrogen and thermally stable under hydrogen at 380 ºC. It was also shown [8] that hydrogen permeation through this alloy is controlled by the atomic diffusion of hydrogen, indicating acceptable surface catalytic activity of this alloy for hydrogen dissociation/recombination. However, hydrogen permeability of this alloy ($1.2–2\times10^{-9}$ mol m^{-1} s^{-1} $Pa^{-0.5}$ at 350 ºC) seems to be considerably lower compared to Pd (~ 1×10^{-8} mol m^{-1} s^{-1} $Pa^{-0.5}$ at 350 ºC) [8]–[10]. Nevertheless, hydrogen permeability of Zr–Ni based alloys was proposed to be [11] dominated by the alloying elements and the alloy composition. A slightly higher hydrogen permeability than Pd was observed as a result of alloying with Nb in $(Ni_{0.6}Nb_{0.4})_{70}Zr_{30}$ alloy (1.3×10^{-8} mol m^{-1} s^{-1} $Pa^{-0.5}$ at 400 ºC) [11]. The hydrogen permeability of Zr–Nb–Ni alloy was strongly dependent on the Zr content of the alloy and further increased in $(Ni_{0.6}Nb_{0.4})_{50}Zr_{50}$ alloy (1.59×10^{-8} mol m^{-1} s^{-1} $Pa^{-0.5}$ at 400 ºC), but at the expense of higher potential for hydrogen embrittlement and a reduced crystallisation temperature [9], [11]–[13]. Multi–component Zr–based amorphous

alloys were studied [14], [15] and hydrogen permeability in the range of 2.3–2.5×10^{-8} mol m^{-1} s^{-1} $Pa^{-0.5}$ at 400 ºC was reported for the $(Ni_{0.6}Nb_{0.4})_{45}Zr_{50}X_5$ (X=Cu, and Co) alloys, almost as high as those of the Pd–Ag alloys [15]. Using first principles calculations, hydrogen solubility and diffusivity in a number of amorphous alloys were predicted and hydrogen permeability suggested to be mainly dominated by hydrogen diffusion in amorphous alloys [16]. Accordingly, $Zr_{54}Cu_{46}$ alloy was predicted to have a hydrogen permeability similar to pure Pd [16], though hydrogen permeability in Zr–Cu alloys was experimentally shown to be lower than computational predictions, possibly due to surface oxidation [17]. Estimations by first principles calculations proposed the maximum achievable hydrogen permeability in amorphous alloys is almost three times higher than pure Pd with $Zr_{30}Cu_{60}X_{10}$ (T= Sc, Ta, Y, and Ti) outperforming $Zr_{54}Cu_{46}$ alloy [18].

The diffusion controlled mechanism in amorphous membranes signifies the possibility of increasing hydrogen permeability by fabricating thinner membranes. Whilst melt spinning seems to be a common method to fabricate amorphous membranes with a typical thickness of 30–50 µm [6], physical vapour deposition offer quick and convenient fabrication methods for the amorphous thin film (<10 µm). Such a method enables the production of amorphous thin films over a wider compositional range with enhanced control over the film shape, size, and thickness. Amorphous Zr–Cu thin films were deposited by magnetron co–sputtering [19], [20] and it was shown that the Glass Forming Ability (GFA) of binary Zr–Cu alloy could be extended to a broader compositional range respecting to other fabrication methods [19]. However, the structure of the films appeared to be sensitive to the sputtering conditions, as low sputtering power, low substrate temperature, and low argon pressure generally encouraged the formation of amorphous thin films [19], [20]. In addition, the thermal behaviour of Zr–Cu and Zr–Ni amorphous alloys showed to be mainly determined by the alloy composition rather than fabrication method [21]–[23]. We recently demonstrated [24]

the possibility of fabricating dense and uniform binary and ternary Zr–based amorphous thin films (< 6 µm) using the Closed Field Unbalanced Magnetron Sputtering Ion Plating (CFUMSIP). Although the thermal stability of these alloys seemed to be dominated by the thin film composition, our preliminary results indicated that the crystallisation process in these amorphous thin films may differ from similar amorphous alloys fabricated by the other methods such as melt spinning [24] . In this study we extend our investigation on $Zr_{36}Ni_{64}$ and $Zr_{54}Cu_{46}$ amorphous thin films, due to their known bulk thermal and crystallisation characteristics [8], [21]–[23] and, $Zr_{30}Cu_{60}Ti_{10}$ and $Zr_{30}Cu_{60}Y_{10}$ amorphous thin films for their predicted comparable hydrogen permeability to pure Pd [16], [18]. Thermal stability of these amorphous thin films under inert and hydrogen atmospheres will be assessed and the possible crystallisation mechanism will be discussed.

2- Materials and method

The sputtering targets (copper, zirconium, nickel, titanium and yttrium – all with 99.9% purity) were purchased from Teer Coatings Ltd. Glass microscope slides (Thermo Scientific) with dimension of 76 × 26 mm were used as substrates for films deposition. Films with varying thicknesses were deposited by the Closed Field Unbalanced Magnetron Sputter Ion Plating (UPD 350–4), and were then peeled off the substrate [24]. The sputtering conditions were optimised after several trial runs to deposit the target $Zr_{36}Ni_{64}$, $Zr_{54}Cu_{46}$, $Zr_{30}Cu_{60}Ti_{10}$ and $Zr_{30}Cu_{60}Y_{10}$ alloys. Whilst the power to the Zr target was varied, all the other sputtering parameters were fixed during each 10 minutes trial run and the optimised sputtering condition for each film is given in Table 1. Low target currents seemed to be necessary to circumvent crystallisation during sputtering. A vacuum level of approximately 10^{-6} mbar was applied to the sputtering chamber and the system was refilled with continuous flow (25 ml/min) of ultra–high purity argon to ~ 2.5×10^{-3} mbar during deposition. Alloys were deposited using pulsed DC with a bias voltage of 50 volts on each magnetron. The target to substrate distance

was kept constant with a sample rotation speed of 5 rpm during the deposition. Each alloy was deposited in 18 runs of 10 min (3 h in total) with a designed cooling period between each run to avoid the temperature raise and possible crystallisation during the deposition process.

Alloys composition and their surface morphology were analysed by a Joel 6060 Scanning Electron Microscope (SEM) equipped with an INCA 300 Energy Dispersive Spectrometer (EDS). Kapton tape was used to partially cover some of the glass substrates during the deposition runs. Kapton tape was removed after deposition and an Ambios Technology XP-200 Profilometer was used for thickness measurements, which the values are included in Table 1.

Room temperature X-Ray Diffraction (XRD) measurements of the films were performed using a Bruker D8–Advanced diffractometer with monochromatic CuKα radiation (λ = 1.54056 Å). Samples were also heat treated at 500 ºC and 650 ºC for 2 h under 3 bar argon and then cooled down to the room temperature before collecting the XRD pattern. An Anton Parr XRK900 high-temperature sample cell was used to measure the temperature dependence crystallisation of each sample under 3 bar flowing helium and hydrogen (100 ml min^{-1}). Samples were heated *in–situ* with a heating rate of 2 $^{\circ}C\ min^{-1}$ from room temperature to 600 ºC (500 ºC under hydrogen) and cooled back to room temperature. The XRD data was refined via a pseudo–Rietveld method with TOPAS Academic software [25] using published crystallographic information files (.cif) obtained from the Inorganic Crystal Systems Database [26].

A Netzsch DSC204HP system was used to perform Differential Scanning Calorimetry (DSC) measurements under 3 bar flowing Ar (100 ml min^{-1}) at heating rates of 2, 5, 10, 15, and 20 °C min^{-1}. DSC measurements were repeated under 3 bar hydrogen (flowing at 100 ml min^{-1}) with a heating rate of 5 °C min^{-1}.

3-Results

3.1 Structural and compositional characterisations

Fig. 1(a–d) shows the XRD pattern of the thin films after deposition on a glass substrate. A broad diffraction hump is observed for all samples within approximately 30º–50º 2θ diffraction angles with no detectable crystalline peaks. This is a common characteristic of amorphous Zr–based thin films as observed in the previous studies [15], [22], [27], [28] regardless of the fabrication method. The formation of an amorphous structure in Zr–based alloys appears to be concentration dependent. For instance, a Cu concentration range of ~ 30–85 at.% is known [22], [23], [27], [28] to encourage the amorphous formation in the Zr–Cu alloy. Hence, the displacement in the diffraction hump's position shown in Fig. 1(a–d) is a result of the composition of the alloys ~~alloys composition~~ and inter–atomic distances within the amorphous matrix. In addition, the broad diffraction hump for Zr–Cu and Zr–Cu–Ti alloys in Fig. 1b and d show~~s~~ a split in the peak, possibly due to phase separation or the partial formation of nano–crystalline phase. Phase separation in the magnetron sputtered Zr–Cu films was observed [31] and suggested that the alloy separated into two amorphous phases with the possible existence of Short Range Order (SRO).The development of such a phase separated structure indicates that the sample temperature during deposition is not high enough to trigger crystallisation of the phase separated region but sufficient for possible atomic mobility particularly on the disposition surface, as a result of kinetics energy, heat of condensation and the heat of mixing of the depositing atoms, which may be somehow overcome by a lower sputtering power and pressure [19],[20], [31].

The surface topographies of the magnetron sputtered alloys are shown in Fig. 2a–d. SEM images show almost featureless growth for all the films. Deposition of continuous films for all the sputtered samples can be observed as it was confirmed in the previous study [24]. Also, the formation of bubble–like structures with diameters of 1–4 µm can be observed on

the films' surfaces. This may be related to the argon entrapment [32] and relaxation of film deposition stresses, leading to the local loss of film–substrate adhesion. Table 1 shows the compositional analysis of the samples by EDS averaging various (at least three readings) area scans (>100 μm^2). It can be seen that the obtained compositions are close to the target compositions, indicating that a good control on the films' compositions can be achieved by accurately controlling the deposition rate of the alloying elements.

3.2 Thermal and structural stability under inert atmosphere

The thermal stabilities of the samples are shown by DSC thermograms in Fig. 3(a–d). All the alloys undergo a crystallisation process above 400 °C as identified by DSC exothermic peaks. The onset and peak temperature of the DSC thermograms can be related to the nucleation and growth processes respectively [9]. Whilst a peak temperature at 467 °C for the crystallisation of $Zr_{40.5}Ni_{59.5}$ alloy can be observed in Fig. 3a, crystallisation peak temperatures around 570 ºC were previously reported for $Zr_{36}Ni_{64}$ alloy [7], [9]. The reduced thermal stability of our sample may be explained by the internal stresses formed during sputtering and its higher Zr content which they both are known to reduce the thermal stability [9], [10], [21]. Furthermore, whilst the crystallisation of $Zr_{40.5}Ni_{59.5}$ (Fig. 3a) takes place through a single exothermic peak, ~~a~~ primary and secondary exothermic peaks were reported [10] during the crystallisation process of melt–spun $Zr_{36}Ni_{64}$. Crystallisation of $Zr_{56.2}Cu_{43.8}$ (Fig. 3b) shows an exothermic reaction with a peak temperature at 461ºC, which is within the range of previously reported crystallisation temperatures [27], [33]–[35]. Crystallisation peak temperatures of 474 and 471 °C can be observed for $Zr_{30}Cu_{57.7}Y_{12.3}$ and $Zr_{32}Cu_{57.3}Ti_{10.7}$ alloys in Fig. 3c and d respectively. A multi-stage crystallisation above 430 °C was observed for the $Zr_{30}Cu_{60}Ti_{10}$ and $Zr_{20}Cu_{60}Ti_{20}$ alloys fabricated by melt spinning [36], [37]. Here, only a broad DSC peak for $Zr_{32}Cu_{57.3}Ti_{10.7}$ alloy (Fig. 3d) can be seen with a possible shoulder at

around 490 °C. These results imply that the crystallisation process in deposited and melt spun Zr–based alloys may follow a dissimilar crystallisation mechanism/path.

The structural stability and the crystallisation products of the samples were also monitored during heating and subsequent cooling to room temperature by *in–situ* XRD in Fig. 4a–d. Stable XRD patterns are observed for the $Zr_{40.5}Ni_{59.5}$ alloy during heating to 400 °C, where zirconium oxide phase evolves. Despite the measurements under flowing helium, elimination of zirconium oxide phases seems to be very difficult due to the high reactivity of zirconium for oxygen (ΔH at 298 K for ZrO_2: -1097.5 kJ mol^{-1}) [17]. Formation of various zirconium oxide phases were observed in the Zr–based alloys, although the quantity of the oxide phase varies according to the alloy composition [17], [23]. In addition, a small amount of Ni phase is formed at 400 °C, which its peak intensity increases upon further heating to 600 °C. Zirconium oxides and Ni are stable phases after cooling to room temperature. It can be seen that crystallisation of the $Zr_{40.5}Ni_{59.5}$ alloy does not proceed by the formation of Ni–Zr phases as expected from the binary phase diagram (Fig. S1 in supporting information) [38] . In fact, decomposition of the amorphous phase has been established in the as–prepared and heat treated amorphous alloys [37], [39], [40]. Amorphous decomposition may force the formation of separated amorphous phases [41], leading to the development of preferential crystallisation (primary crystallisation) from such phases. In addition, Zr content may have been also depleted as a result of oxidation. Hence, amorphous decomposition and oxidation of the $Zr_{40.5}Ni_{59.5}$ alloy observed in Fig. 4a seems to have encouraged the formation of Ni–rich zones which are preferentially crystallised upon heating.

A split in the XRD peak for the $Zr_{56.2}Cu_{43.8}$ alloy (also showed in Section 3.1) almost disappears once the alloy is heated to 200 °C in Fig. 4b, possibly due to thermal expansion. Crystallisation starts at 300 °C by the formation of a minute amount of Cu and zirconium

oxide phases which their XRD peak intensities increase by heating to 600 °C. At 600 °C, a mixture of Zr_2Cu, Zr_7Cu_{10}, and $Zr_{14}Cu_{51}$ phases are also observed in combination with the aforementioned phases. The structure of the $Zr_{56.2}Cu_{43.8}$ alloy after cooling to room temperature remains similar to the heat treated sample at 600 °C. According to the Cu–Zr phase diagram (Fig. S2 in supporting information) [42], a mixture of Zr_2Cu and Zr_7Cu_{10} phases should be the dominant phases after the crystallisation of this alloy. In fact, crystallisation of Zr–Cu alloys with a Zr content ranging from 45 to 60 at.% was shown to proceed by the formation of a mixture of Zr_2Cu and Zr_7Cu_{10} phases [27], [34]. Meanwhile, formation of the $Zr_{14}Cu_{51}$ phase was only observed for Zr–Cu alloys with a Zr content lower than 40 at.% [23]. Evolution of the $Zr_{14}Cu_{51}$ phase in our sample may originate from the variation in the local atomic composition as a result of the separation of Cu–rich zones (Zr–poor zones) [37] which its preferential crystallisation can be seen in Fig. 4b. Phase separation in the Zr–Cu alloys was reported to occur during the alloy fabrication by vapour quenching [43] and after annealing at temperatures far below the glass transition for the liquid quenched alloys [31]. In addition, competition between the separated Cu phase for surface segregation due to its lower surface energy compared to Zr (1.83 J m^{-2} vs. 2 J m^{-2}) [44] and the selective oxidation of Zr can magnify changes in the local atomic composition.

No significant changes in the XRD patterns of the $Zr_{30}Cu_{57.7}Y_{12.3}$ alloy are~~is~~ observed in Fig. 4c until heating to 400 °C, where zirconium oxide and Cu phases are formed. $Zr_{14}Cu_{51}$ and Zr_7Cu_{10} phases are also formed by a further increase in the temperature to 600 °C. The structure of the $Zr_{30}Cu_{57.7}Y_{12.3}$ alloy remains unchanged after cooling to room temperature. Similar to the $Zr_{30}Cu_{57.7}Y_{12.3}$ alloy, the formation of zirconium oxide and Cu phases are observed for the $Zr_{32}Cu_{57.3}Ti_{10.7}$ alloy after heating to 400 °C in Fig. 4d which their peaks intensify with an increase in temperature. However, only a small amount of $Zr_{14}Cu_{51}$ phase forms by heating to 600 °C. Formation of the $Zr_{14}Cu_{51}$ phase was also observed from 450 °C

in the first crystallisation stage of the $Zr_{20}Cu_{60}Ti_{20}$ ribbon [37]. Cooling the $Zr_{32}Cu_{57.3}Ti_{10.7}$ alloy to room temperature has no noticeable effect on the structure of the alloy.

Table 2 shows crystal structure refinement results for the samples heat treated at 500 and 650 °C under argon for 2 h (Fig. S3–S6 in supporting information). A significant amount of Ni (about 66 wt. %) is crystallised after heat treating $Zr_{40.5}Ni_{59.5}$ alloy at 500 °C. The phase abundance of Ni decreases after heat treating at 650 °C due to an increase in the quantity of oxide phases. The absence of a Zr–Ni phase after heat treatment at 650 °C seems to be related to the alloy decomposition. Crystallisation of the separated Ni phase and the Zr consumption by oxygen hinder the intermetallic compounds precipitation. Heat treatment of the $Zr_{56.2}Cu_{43.8}$ alloy at 500 °C results in crystallisation of zirconium oxides, Cu and Zr_7Cu_{10} phases. The phase abundance of Cu decreases from 15 to 8 wt. % after increasing the heat treatment temperature from 500 to 650 °C which is also accompanied by the formation of Zr_2Cu and $Zr_{14}Cu_{51}$ phases. It has been suggested that thermodynamics imposes preferential formation of the $Zr_{14}Cu_{51}$ phase from Cu–rich zones, leading to Cu depletion [23]. The phase abundance of Cu is about 14 wt. % after heat treating the $Zr_{30}Cu_{57.7}Y_{12.3}$ alloy at 500 °C. The separated Cu phase seems to be completely consumed at 650 °C as a result of $Zr_{14}Cu_{51}$ phase enrichment which was previously formed at 500 °C. Similarly, the crystallised Cu with a phase abundance of about 18 wt. % is completely consumed at the expense of $Zr_{14}Cu_{51}$ phase enrichment in the $Zr_{32}Cu_{57.3}Ti_{10.7}$ alloy after increasing the heat treatment temperature from 500 to 650 °C. Thus, it seems that phase separation and oxidation in these alloys (particularly $Zr_{40.5}Ni_{59.5}$ and $Zr_{56.2}Cu_{43.8}$ alloys) can potentially alter the crystallisation path/ products. Furthermore, quantitative phase analyses on the $Zr_{56.2}Cu_{43.8}$, $Zr_{30}Cu_{57.7}Y_{12.3}$ and $Zr_{32}Cu_{57.3}Ti_{10.7}$ alloys suggests that Cu phase separation seems to be less significant in the $Zr_{30}Cu_{57.7}Y_{12.3}$ and $Zr_{32}Cu_{57.3}Ti_{10.7}$ alloys, despite their higher Cu content. This may originate from the Y and Ti additions to the binary alloy.

3.3 Thermal stability under hydrogen

The effects of hydrogen on thermal stability of the alloys in this study are shown by DSC thermograms in Fig. 5(a–d). The DSC thermogram for the $Zr_{40.5}Ni_{59.5}$ alloy in Fig. 5a shows two exothermic peaks at low (90 °C) and high temperatures (458 °C). The high temperature DSC peak is very close to the exothermic peak temperature observed for the crystallisation of this alloy under an inert atmosphere (467 °C) in Fig. 3a. $Zr_{56.2}Cu_{43.8}$ alloy shows (Fig. 5b) a wide exothermic DSC thermogram starting from approximately 125 °C with a peak temperature at 279 °C. Therefore, the thermal stability of this alloy seems to be drastically reduced under hydrogen compared to its thermal stability under argon in Fig. 3b. Similar reductions in thermal stability of Zr–Cu alloys under hydrogen were also previously reported as a result of ZrH_2 and Cu phase formation at temperatures lower than the crystallisation temperature of the alloys [6], [33]. The same trend is also observed for the $Zr_{30}Cu_{57.7}Y_{12.3}$ and $Zr_{32}Cu_{57.3}Ti_{10.7}$ alloys as their thermal stabilities are significantly lower under hydrogen (Fig. 5c–d), compared to their thermal stability under argon (Fig. 3c–d). Whilst the $Zr_{30}Cu_{57.7}Y_{12.3}$ alloy shows two exothermic peaks in Fig. 5c with peak temperatures at 160 and 245 °C, a wide exothermic peak starting from approximately 100 °C and a peak temperature at 290 °C is observed for the $Zr_{32}Cu_{57.3}Ti_{10.7}$ alloy in Fig. 5d. The observed reductions in the thermal stabilities under hydrogen may arise from enhanced atomic mobility allowing easier rearrangement into the crystalline phase, hydrogen induced phase separation and localised heating during hydriding, all of which appear to be a function of hydrogen concentration within the alloy [6], [45].

The *in–situ* XRD at variable temperatures (Fig. 6a–d) shows the structural stability and the crystallisation products of the samples under hydrogen. The XRD pattern of the $Zr_{40.5}Ni_{59.5}$ alloy in Fig. 6a seems to remain unchanged after heating to 150 °C. Therefore, the low temperature DSC exothermic peak at 90 °C which was observed for this alloy in Fig. 5a

cannot be related to alloy crystallisation. An exothermic peak for hydrogen absorption in $Z_{37}Ni_{63}$ alloy was reported [46] below 200 °C, which was accompanied by a shift in the broad XRD diffraction hump to the lower angle side as result of volume expansion. Such a shift in the broad XRD diffraction hump is not observed after careful examination of Fig. 6a once the temperature increases to 150 °C. On the other hand, the low temperature DSC exothermic peak may be related to partial oxidation, in which the oxide layer is too thin to be identified by XRD. Formation of tetragonal ZrO_2 can be clearly observed in Fig. 6a after heating the $Zr_{40.5}Ni_{59.5}$ alloy above 350 °C. Crystallisation of the Ni phase is detected at 450 °C in combination with tetragonal ZrO_2 as the main oxide phase. Formation of ZrH_2 is not observed in this sample at the current experimental conditions, despite the porous nature of tetragonal ZrO_2 [46]. Thus, the high temperature DSC exothermic peak (458 °C) in Fig. 5a should represent the crystallisation of the $Zr_{40.5}Ni_{59.5}$ alloy under hydrogen which seems to be relatively unaffected compared to the $Zr_{40.5}Ni_{59.5}$ alloy crystallisation under an inert atmosphere (467 °C). No changes in the XRD pattern of the $Zr_{56.2}Cu_{43.8}$ alloy are detected until 250 °C, where crystallisation of ZrH_2 and Cu are observed. Therefore, the broad exothermic DSC shoulder below this temperature (Fig. 5b) cannot be related to the alloy crystallisation, rather possible structural relaxation or some reordering of the amorphous structure [33]. Similarly, decomposition of Zr–Cu alloys under hydrogen was reported to proceed by phase separation leading to the formation of ZrH_2, Cu and Cu–Zr phases [33], [45], [47]. Such a structural transformation under hydrogen induced fast Cu segregation to the surface [47]. An additional increase in temperature to 500 °C in Fig. 6b results in the growth of XRD peak intensities for ZrH_2 and Cu and the formation of a small amount of Zr oxide phases. The XRD pattern of the $Zr_{30}Cu_{57.7}Y_{12.3}$ and $Zr_{32}Cu_{57.3}Ti_{10.7}$ alloys remain unchanged in Fig. 6c–d until 200 °C. Hence, similar to the $Zr_{56.2}Cu_{43.8}$ alloy, the first exothermic peak for the $Zr_{30}Cu_{57.7}Y_{12.3}$ alloy in Fig. 5c may be related to the structural

relaxation or some atomic rearrangement in the amorphous structure. Decomposition of the amorphous structure to ZrH_2 and Cu phases commences for both $Zr_{30}Cu_{57.7}Y_{12.3}$ and $Zr_{32}Cu_{57.3}Ti_{10.7}$ after heating the alloys to 250 °C which is in good agreement with their DSC profiles in Fig. 5c–d. Whilst the XRD peak intensities of ZrH_2 and Cu increase for the $Zr_{30}Cu_{57.7}Y_{12.3}$ alloy after heating to 500 °C in Fig. 6c, decomposition of Cu (which starts at ~ 250 °C) appears to be the main crystallisation event in the $Zr_{32}Cu_{57.3}Ti_{10.7}$ alloy after heating to 500 °C in Fig. 6d. A small amount of the Zr oxide phase is also detected in both of the alloys at the end of the heating and cooling cycle. Similar to the crystallisation profiles of the alloys under an inert atmosphere, a notable phase separation is observed during the crystallisation of these alloys under hydrogen.

4 Discussion

Since crystallisation is associated with nucleation and growth, the kinetic studies of nucleation and growth processes in amorphous alloys are important. The crystallisation kinetics of amorphous materials can be investigated using isothermal or non–isothermal methods [48]. Whilst most kinetic investigations are performed isothermally, the substantial thermal response of the amorphous alloys in this study causes the nucleation and growth process to occur before the alloy reaches the desired temperature. On the other hand, in the non–isothermal method sample is heated at a fixed heating rate until crystallisation is complete. Whilst the Johnsdon–Mehl–Avrami (JMA) theory [49], [50] can be used to describe the crystallisation kinetics during isothermal measurements, other theories have been developed [48] to obtain the kinetics parameters for glass crystallisation based on non–isothermal methods. In non–isothermal measurements the kinetic parameters are obtained by monitoring the shift in the crystallisation peak as a function of heating rate [51].

Ozawa [52] and Kissinger [53] plots are commonly used methods to calculate the kinetics data, such as Avrami exponent, n, and activation energy, E_a, by non–isothermal

measurements. The Avrami exponent represents the growth morphology [48] depending on the growth mechanism, *i.e.* dimensionality of growth and the growth limiting factors such as diffusion or surface controlled growth [48], [54]. The Avrami exponent, *n,* is determined by the Ozawa equation (eq. 1), whilst the activation energies for nucleation and growth can be determined from onset and peak temperatures of the DSC thermograms respectively at different heating rates [9], [24] using the Kissinger equation (Eeq. 2).

$$\ln\left[-\ln\left(1-x\right)\right] = -n\ln\beta + Constant \qquad \text{Eeq. (1)}$$

$$\frac{d\ln\left(\frac{\beta}{T_p^2}\right)}{d\left(\frac{1}{T_p}\right)} = -\frac{E_a}{R} \qquad \text{Eeq. (2)}$$

Where x is the crystallised fraction, determined from the ratio of total area of the exothermic crystallisation peak to the partial area of the exothermic crystallisation peak with respect to the starting and finishing crystallisation temperature [48]. β is the heating rate, T_p is the crystallisation peak temperature (crystallisation onset temperature to calculate the activation energy for nucleation) and R is the gas constant.

The sigmoid graphs in Fig. 7a–d represent the crystallised fraction of the alloys in this study with respect to the temperature, calculated from the DSC measurements at different heating rates. The inset graphs are plots of *ln[-ln(1-x)]* vs. *lnβ* at different temperatures to calculate the average Avrami exponent, *n,* by least squares fitting according to the Ozawa method (*n* values also given in Table 1). The average *n* values of 1.93 and 1.29 are determined in Fig. 7a–b for the $Zr_{40.5}Ni_{59.5}$ and $Zr_{56.2}Cu_{43.8}$ alloys respectively. Whilst the integer values from 1 to 4 for the Avrami exponent represents a surface or bulk crystallisation, the non–integer values of the Avrami exponent may be attributed to the coexistence of surface and bulk crystallisation and because of the consequences of several complex processes occurring during the growth of a particular phase [51]. The Avrami exponent close to 2 for the $Zr_{40.5}Ni_{59.5}$ alloy indicates one dimensional growth of the crystals

within the bulk of the alloy with constant nucleation [48]. On the other hand, the Avrami exponent close to 1 for the $Zr_{56.2}Cu_{43.8}$ alloy suggests surface crystallisation [48]. In Section 3.2 we showed that decomposition of the amorphous phase results in the Ni and Cu phase separation during the crystallisation of $Zr_{40.5}Ni_{59.5}$ and $Zr_{56.2}Cu_{43.8}$ alloys. Despite the Cu tendency for surface segregation, it is less likely for Ni to segregate to the surface due to its higher surface energy compared to Zr (2.45 J m^{-2} vs. 2 J m^{-2}) [44]. Therefore, the bulk crystallisation suggested by the Avrami exponent for $Zr_{40.5}Ni_{59.5}$ applies to the crystallisation of Ni within the bulk of this alloy, whilst the crystallisation of the segregated Cu on the surface dominates the crystallisation of $Zr_{56.2}Cu_{43.8}$ alloy. The Avrami exponent values of 1.93 and 1.75 are determined for the $Zr_{30}Cu_{57.7}Y_{12.3}$ and $Zr_{32}Cu_{57.3}Ti_{10.7}$ alloys in Fig. 7c–d which indicates (based on the non–integer value) one dimensional growth of the crystals within the bulk of the alloy with constant nucleation, similar to the $Zr_{40.5}Ni_{59.5}$ alloy. This is in a good agreement with our proposition in Section 3.2 denoting that Cu phase separation is less significant in the $Zr_{30}Cu_{57.7}Y_{12.3}$ and $Zr_{32}Cu_{57.3}Ti_{10.7}$ alloys compared to the $Zr_{56.2}Cu_{43.8}$ alloy, despite the higher Cu content in the ternary alloys. In fact, it was shown in Table 2 that the separated Cu phase is involved in the intermetallic precipitation as the crystallisation process proceeds. Besides the lower scale of Cu phase separation in the $Zr_{30}Cu_{57.7}Y_{12.3}$ and $Zr_{32}Cu_{57.3}Ti_{10.7}$ alloys, Cu does not seem to significantly segregate to the surface possibly due to the limited atomic diffusion as a result of Y [55] and Ti additions. Therefore, it seems that Cu segregation is considerably alleviated in the $Zr_{30}Cu_{57.7}Y_{12.3}$ and $Zr_{32}Cu_{57.3}Ti_{10.7}$ alloys compared to the $Zr_{56.2}Cu_{43.8}$ alloy, hence encouraging bulk crystallisation rather than surface crystallisatoin.

Activation energies for crystallisation (nucleation and growth) of the alloys in this study are given in Fig. 8a–d (also listed in Table 1). The activation energies for nucleation of the $Zr_{40.5}Ni_{59.5}$ and $Zr_{56.2}Cu_{43.8}$ alloys are 287.1 and 418.7 kJ mol^{-1} respectively. These values are

higher than the calculated activation energies for growth in the $Zr_{40.5}Ni_{59.5}$ (234.5 kJ mol^{-1}) and $Zr_{56.2}Cu_{43.8}$ (395.9 kJ mol^{-1}) alloys given in Fig. 8a and b, indicating that more energy is required for nucleation process compared to the growth process in these alloys. The reverse seems to apply for the $Zr_{30}Cu_{57.7}Y_{12.3}$ and $Zr_{32}Cu_{57.3}Ti_{10.7}$ alloys in Fig. 8 c and d, where the activation energies for nucleation (347.2 and 284.8 kJ mol^{-1}) are considerably lower than the activation energies of growth (415.5 and 395.6 kJ mol^{-1}), indicating that the growth process is more difficult than the nucleation process in these alloys.

The mechanical and physical properties of amorphous alloys are known to be related to the atomic packing density, defined by the formation of atomic clusters exhibiting Short Range Order [56], [57]. In addition, recent studies show that the structural stability (assessed by the crystallisation temperature) of amorphous alloys is also closely related to the characteristics of the SRO atomic clusters [35], [57]–[59]. For multicomponent systems where the constituent atoms exhibit a notable difference in their atomic sizes, the most efficient packing occurs locally in icosahedra–like clusters [60] without long translational symmetry. Zr–based metallic glasses also tend to form icosahedra–like atomic clusters in order to promote better packing density [61]. For instance, the GFA and the thermal stability of Zr–Cu amorphous alloys have been shown to depend on the fraction of Cu– centred full icosahedra–like clusters [35], [58], [62]. Thermal stability was observed to originate from significantly lower atomic mobility of atoms belonging to the full icosahedra–like clusters [62]. However, the nature of the icosahedra–like clusters is a function of the alloy composition and the atomic species. The existence of multiple atomic species with different atomic sizes can change the chemical environment, leading to lower packing density and a deterioration in thermal stability by limiting the formation of full icosahedra–like clusters [59], [63], [64]. Such an effect has been reported after micro–alloying of Ti [65], and Y [55] with the Zr–Cu based amorphous alloys. Whilst a small atomic mismatch between Ti and the

base alloy elements was suggested [65] to result in lower packing efficiency, the positive enthalpy of mixing between Y and Zr (+35 kJ mol^{-1}) could lead to a local variation in the alloy composition [55]. Furthermore, the formation of crystal–like structures [55] were shown to be likely as a result of micro–alloying, which can act as the crystallisation nuclei. However, the growth of thisese crystal–like structures remains limited to a few nm during crystallisation and the overall rate of crystallisation is reduced. This is mainly attributed to the pinning effect of the surrounding icosahedra–like clusters [55], [61], which promote nano–crystallisation in Zr–based amorphous alloys. The higher nucleation activation energies in the $Zr_{40.5}Ni_{59.5}$ and $Zr_{56.2}Cu_{43.8}$ alloys compared to their growth activation energies may arise from the fact that icosahedra–like clusters remain almost unchanged during the early stages of the crystallisation. Short range ordered metastable icosahedra–like clusters can greatly reduce the system's potential and slow down the crystal nucleation kinetic [61]. When the initial icosahedra–like clusters collapse, crystal growth becomes easier in accordance to the calculated growth activation energies for these alloys. The lower nucleation activation energies for $Zr_{30}Cu_{57.7}Y_{12.3}$ and $Zr_{32}Cu_{57.3}Ti_{10.7}$ alloys compared to their growth activation energies denote that Y and Ti additions may have reduced the packing density and encouraged the formation of crystal–like structures that can facilitate the nucleation process. Nevertheless, the growth process for this crystal–like structures is still difficult, possibly due to the pinning effect of the surrounding icosahedra–like clusters which is reflected by the growth activation energies in these alloys.

5. Conclusions

Amorphous thin films of $Zr_{40.5}Ni_{59.5}$, $Zr_{56.2}Cu_{43.8}$, $Zr_{30}Cu_{57.7}Y_{12.3}$, and $Zr_{32}Cu_{57.3}Ti_{10.7}$ as potential hydrogen separation membranes were fabricated by the magnetron sputtering method. The crystallisation process in these alloys under an inert atmosphere only starts after increasing the temperature above 400 ^{o}C. Whilst $Zr_{40.5}Ni_{59.5}$ showed a comparable thermal

stability under hydrogen and an inert atmosphere, the thermal stability of $Zr_{56.2}Cu_{43.8}$, $Zr_{30}Cu_{57.7}Y_{12.3}$, and $Zr_{32}Cu_{57.3}Ti_{10.7}$ alloys was significantly reduced under hydrogen. Structural analysis indicated oxidation and decomposition of amorphous phase under hydrogen and an inert atmosphere during the crystallisation process, leading to phase separation, particularly Ni and Cu in the $Zr_{40.5}Ni_{59.5}$ and $Zr_{56.2}Cu_{43.8}$ alloys. However, the scale of Cu phase separation appears to be lower in the $Zr_{30}Cu_{57.7}Y_{12.3}$, and $Zr_{32}Cu_{57.3}Ti_{10.7}$ alloys, despite their higher Cu content compared to the $Zr_{56.2}Cu_{43.8}$ alloy. Phase separation seems to change the local atomic structure, hence influencing the crystallisation path and products. Kinetic studies by non–isothermal measurements suggest that the high tendency of separated Cu for surface segregation encourages surface crystallisation in the $Zr_{56.2}Cu_{43.8}$ alloy, whereas the crystallisation process is dominated by the nucleation and growth of crystals within the bulk of the other alloys in this study. According to the calculated activation energies, it is suggested that the existence of the SRO metastable icosahedra–like clusters may make the nucleation process more difficult in the $Zr_{40.5}Ni_{59.5}$ and $Zr_{56.2}Cu_{43.8}$ alloys compared to the growth process. A reverse trend seems to apply in the case of $Zr_{30}Cu_{57.7}Y_{12.3}$ and $Zr_{32}Cu_{57.3}Ti_{10.7}$ alloys as Y and Ti additions may reduce the packing density as a result of atomic size mismatch and change in the local atomic structure, thus encouraging the formation of crystal–like structures that can act as nucleation sites. However, the higher activation energies calculated for the growth process of these alloys suggest growth difficulties for the crystal–like structures possibly due to the pinning effect of the surrounding icosahedra–like clusters. Despite the reported comparable hydrogen permeability of $Zr_{56.2}Cu_{43.8}$, Zr_{30} $Cu_{57.7}Y_{12.3}$ and $Zr_{32}Cu_{57.3}Ti_{10.7}$ alloys to Pd, their poor thermal stability under hydrogen seems to limit the application of these alloys as hydrogen purification membranes.

Acknowledgments

Supports from the EPSRC SUPERGEN Delivery of Sustainable Hydrogen (EP/G01244X/1), the Birmingham Science City Hydrogen Energy projects and the Hydrogen and Fuel Cell Research Hub are gratefully acknowledged.

References

[1] M. D. Dolan, "Non-Pd BCC alloy membranes for industrial hydrogen separation," *J. Memb. Sci.*, vol. 362, no. 1–2, pp. 12–28, 2010.

[2] J. W. Phair and R. Donelson, "REVIEWS Developments and Design of Novel (Non-Palladium-Based) Metal Membranes for Hydrogen Separation," *Ind. Eng. Chem. Res., vol.* 45, pp. 5657–5674, 2006.

[3] N. W. Ockwig and T. M. Nenoff, "Membranes for Hydrogen Separation Membranes for Hydrogen Separation," *Chem.Rev.*, vol. 107, no. 10, pp. 4078–4110, 2007.

[4] S. Hao and D. S. Sholl, "Using first-principles calculations to accelerate materials discovery for hydrogen purification membranes by modeling amorphous metals," *Energy Environ. Sci.*, vol. 1, no. 1, p. 175, 2008.

[5] S. Hao, M. Widom, and D. S. Sholl, "Probing hydrogen interactions with amorphous metals using first-principles calculations.," *J. Phys. Condens. Matter*, vol. 21, no. 11, p. 115402, 2009.

[6] M. D. Dolan, N. C. Dave, a. Y. Ilyushechkin, L. D. Morpeth, and K. G. McLennan, "Composition and operation of hydrogen-selective amorphous alloy membranes," *J. Memb. Sci.*, vol. 285, no. 1–2, pp. 30–55, Nov. 2006.

[7] M. D. Dolan, S. Hara, N. C. Dave, K. Haraya, M. Ishitsuka, a. Y. Ilyushechkin, K. Kita, K. G. McLennan, L. D. Morpeth, and M. Mukaida, "Thermal stability, glass-forming ability and hydrogen permeability of amorphous Ni64Zr36−XMX (M=Ti, Nb, Mo, Hf, Ta or W) membranes," *Sep. Purif. Technol.*, vol. 65, no. 3, pp. 298–304, Mar. 2009.

[8] S. Hara, K. Sakaki, N. Itoh, H.-M. Kimura, K. Asami, and a. Inoue, "An amorphous alloy membrane without noble metals for gaseous hydrogen separation," *J. Memb. Sci.*, vol. 164, no. 1–2, pp. 289–294, 2000.

[9] S. M. Kim, D. Chandra, N. K. Pal, M. D. Dolan, W. M. Chien, A. Talekar, J. Lamb, S. N. Paglieri, and T. B. Flanagan, "Hydrogen permeability and crystallization kinetics in amorphous Ni-Nb-Zr alloys," *Int. J. Hydrogen Energy*, vol. 37, no. 4, pp. 3904–3913, 2012.

[10] M. Dolan, N. Dave, L. Morpeth, R. Donelson, D. Liang, M. Kellam, and S. Song, "Ni-based amorphous alloy membranes for hydrogen separation at 400°C," *J. Memb. Sci.*, vol. 326, no. 2, pp. 549–555, Jan. 2009.

[11] S. I. Yamaura, Y. Shimpo, H. Okouchi, M. Nishida, O. Kajita, H. Kimura, and A. Inoue, "Hydrogen permeation characteristics of melt-spun Ni-Nb-Zr amorphous alloy

membranes," *Mater. Trans.*, vol. 44, no. 9, pp. 1885–1890, 2003.

[12] S. N. Paglieri, N. K. Pal, M. D. Dolan, S. M. Kim, W. M. Chien, J. Lamb, D. Chandra, K. M. Hubbard, and D. P. Moore, "Hydrogen permeability, thermal stability and hydrogen embrittlement of Ni-Nb-Zr and Ni-Nb-Ta-Zr amorphous alloy membranes," *J. Memb. Sci.*, vol. 378, no. 1–2, pp. 42–50, 2011.

[13] S. I. Yamaura, M. Sakurai, M. Hasegawa, K. Wakoh, Y. Shimpo, M. Nishida, H. Kimura, E. Matsubara, and A. Inoue, "Hydrogen permeation and structural features of melt-spun Ni-Nb-Zr amorphous alloys," *Acta Mater.*, vol. 53, no. 13, pp. 3703–3711, 2005.

[14] S. Yamaura, S. Nakata, H. Kimura, Y. Shimpo, M. Nishida, and A. Inoue, "Hydrogen Permeation of the Melt-Spun Ni–X–Zr Amorphous Membranes," *Mater. Trans.*, vol. 46, no. 8, pp. 1768–1770, 2005.

[15] S. I. Yamaura, Y. Shimpo, H. Okouchi, M. Nishida, O. Kajita, and A. Inoue, "The effect of additional elements on hydrogen permeation properties of melt-spun Ni-Nb-Zr amorphous alloys," *Mater. Trans.*, vol. 45, no. 2, pp. 330–333, 2004.

[16] S. Hao and D. S. Sholl, "Computational prediction of durable amorphous metal membranes for H2 purification," *J. Memb. Sci.*, vol. 381, no. 1–2, pp. 192–196, Sep. 2011.

[17] T. Lai, H. Yin, and M. Laura Lind, "The hydrogen permeability of Cu-Zr binary amorphous metallic membranes and the importance of thermal stability," *J. Memb. Sci.*, vol. 489, pp. 264–269, 2015.

[18] S. Hao and D. S. Sholl, "Rapid prediction of hydrogen permeation through amorphous metal membranes: an efficient computational screening approach," *Energy Environ. Sci.*, vol. 6, no. 1, p. 232, 2013.

[19] J. Qin, X. U. Y. M, Z. Xin-Yu, L. I. G. Û, L. I. Li-Xin, X. Yong, Z. Xin-Yu, L. Gong, L. I. Li-Xin, X. Zhe, M. Ming-Zhen, and L. Ri-Ping, "Zr-Cu Amorphous Films Prepared by Magnetron Co-sputtering Deposition of Pure Zr and Cu," *Chinese Phys. Lett.*, vol. 26, no. 8, p. 086109, 2009.

[20] C. J. Chen, J. C. Huang, H. S. Chou, Y. H. Lai, L. W. Chang, X. H. Du, J. P. Chu, and T. G. Nieh, "On the amorphous and nanocrystalline Zr-Cu and Zr-Ti co-sputtered thin films," *J. Alloys Compd.*, vol. 483, pp. 337–340, 2009.

[21] K. Coulter and D. Driscoll, "II . D . 4 Amorphous Alloy Membranes for High Temperature Hydrogen Separation Technical Targets," *DOE Hydrog. Program, Annu. Prog. Rep.*, pp. 86–89, 2010.

[22] M. Apreutesei, P. Steyer, L. Joly-Pottuz, a. Billard, J. Qiao, S. Cardinal, F. Sanchette, J. M. Pelletier, and C. Esnouf, "Microstructural, thermal and mechanical behavior of co-sputtered binary Zr-Cu thin film metallic glasses," *Thin Solid Films*, vol. 561, pp. 53–59, 2014.

[23] M. Apreutesei, P. Steyer, a. Billard, L. Joly-Pottuz, and C. Esnouf, "Zr–Cu thin film metallic glasses: An assessment of the thermal stability and phases' transformation mechanisms," *J. Alloys Compd.*, vol. 619, pp. 284–292, 2015.

[24] S. Nayebossadri, D. Smith, J. Speight, and D. Book, "Amorphous Zr-based thin films

fabricated by magnetron sputtering for potential application in hydrogen purification," *J. Alloys Compd.*, vol. 645, pp. S56–S60, 2015.

[25] A. Coelho, "Topas-Academic, Version 4.1, Coelho Software, Brisbane, Australia," 2007.

[26] D. A. Fletcher, R. F. McMeeking, and D. Parkin, "The United Kingdom Chemical Database Service," *J. Chem. Inf. Model.*, vol. 36, no. 4, pp. 746–749, 1996.

[27] H. R. Wang and Y. F. Ye, "Crystallization processes in amorphous Zr 54 Cu 46 alloy," vol. 311, pp. 36–41, 2002.

[28] K.-W. Park, J.-P. Ahn, H.-K. Seok, and Y.-C. Kim, "Relationship between activation energy for hydrogen permeation and hydrogen permeation properties of amorphous Cu50Zr50 and Cu65Zr35 membranes," *Intermetallics*, vol. 19, no. 12, pp. 1887–1890, Dec. 2011.

[29] L. Xie, P. Brault, A. L. Thomann, and L. Bedra, "Molecular dynamic simulation of binary ZrxCu100-x metallic glass thin film growth," *Appl. Surf. Sci.*, vol. 274, pp. 164–170, 2013.

[30] K. Kondoh, J. Fujita, J. Umeda, and T. Serikawa, "Estimation of Compositions of Zr-Cu Binary Sputtered Film and Its Characterization," *Adv. Mater. Sci. Eng.*, vol. 2008, pp. 1–5, 2008.

[31] T. W. Barbee, "Phase separation in vapor quench synthesized noncrystalline copper zirconium alloys," *Appl. Phys. Lett.*, vol. 38, no. 3, p. 132, 1981.

[32] B. R. Chalamala and R. H. Reuss, "Argon inclusion in sputtered films and the effect of the gas on molybdenum field emitter arrays," *Appl. Phys. Lett.*, vol. 78, no. 2001, pp. 2151–2153, 2001.

[33] R. A. D. K. Dinin, "Crystallisation and hydrogen absorption in amorphous Cu60Zr40 and Cu50Zr50," *J. Phys. F Met. Phys.*, vol. 15, pp. 273–277, 1985.

[34] Z. Altounian, "Crystallization characteristics of Cu-Zr metallic glasses from Cu70Zr30 to Cu25Zr75," *J. Appl. Phys.*, vol. 53, no. 7, p. 4755, 1982.

[35] B. F. Lu, J. F. Li, L. T. Kong, and Y. H. Zhou, "Correlation between mechanical behavior and glass forming ability of Zr-Cu metallic glasses," *Intermetallics*, vol. 19, pp. 1032–1035, 2011.

[36] K. K. A. Inoue, W. Zhang, T. Zhang, "Thermal and Mechanical Properties of Cu-Based Cu-Zr-Ti Bulk Glassy Alloys.," *Mater. Trans.*, vol. 42, no. 6, p. 1149, 2001.

[37] A. Concustell, Á. Révész, S. Suriñach, L. K. Varga, G. Heunen, and M. D. Baró, "Microstructural evolution during decomposition and crystallization of the Cu60Zr20Ti20 amorphous alloy," *J. Mater. Res.*, vol. 19, pp. 505–512, 2004.

[38] N. Wang, C. Li, Z. Du, and F. Wang, "Experimental study and thermodynamic re-assessment of the Ni-Zr system," *Calphad Comput. Coupling Phase Diagrams Thermochem.*, vol. 31, no. 4, pp. 413–421, 2007.

[39] C. Antonione, S. Spriano, P. Rizzi, M. Baricco, and L. Battezzati, "Phase separation in multicomponent amorphous alloys," *J. Non. Cryst. Solids*, vol. 232–234, pp. 127–132, 1998.

[40] R. Busch, S. Schneider, a. Peker, and W. L. Johnson, "Decomposition and primary crystallization in undercooled Zr 41.2Ti13.8Cu12.5Ni10.0Be 22.5 melts," *Appl. Phys. Lett.*, vol. 67, no. 1995, p. 1544, 1995.

[41] S. C. Glade, J. F. Löffler, S. Bossuyt, W. L. Johnson, and M. K. Miller, "Crystallization of amorphous Cu47Ti34Zr11Ni8," *J. Appl. Phys.*, vol. 89, no. 3, pp. 1573–1579, 2001.

[42] H. Okamoto, "Cu-Zr (Copper-Zirconium)," *J. Phase Equilibria Diffus.*, vol. 33, no. 5, pp. 1–2, 2012.

[43] R. Schulz, K. Samwer, and W. L. Johnson, "Kinetics of Phase Separation in Cu50Zr50 Metallic Glasses," *J. Non-*, vol. 61 & 62, pp. 997–1002, 1984.

[44] N. M. R. H.L. Skriver, "Surface energy and work function of elemental metal." pp. 7157–7168, 1992.

[45] N. Eliaz and D. Eliezer, "An Overview of Hydrogen Interaction with Amorphous Alloys," *Adv. Perform. Mater.*, vol. 31, pp. 5–31, 1999.

[46] K. Aoki, T. Masumoto, and C. Suryanarayana, "Crystallization of amorphous Zr-Ni alloys in the presence of H/sub 2/, CO, O/sub 2/, N/sub 2/ and argon gases," *J. Mater. Sci.*, vol. 21, no. 3, pp. 793–798, 1986.

[47] T. Katona, A. Molnar, I. V. Perczel, C. Kopasz, and Z. Hegedüs, "Changes Induced in the Surface Characteristics and Catalytic Activity of Amorphous Cu-Zr," *Surf. Interface Anal.*, vol. 19, pp. 519–523, 1992.

[48] M. Çelikbilek, A. E. Erdundu, and S. Aydin, "Crystallization Kinetics of Amorphous Materials," *Adv. Cryst. …*, 2012.

[49] M. Avrami, "Kinetics of Phase Change. I General Theory," *J. Chem. Phys.*, vol. 7, no. 12, p. 1103, 1939.

[50] M. Avrami, "Kinetics of Phase Change. II Transformation-Time Relations for Random Distribution of Nuclei," *J. Chem. Phys.*, vol. 8, no. 2, p. 212, 1940.

[51] M. Çelikbilek, a. E. Ersundu, N. Solak, and S. Aydin, "Crystallization kinetics of the tungsten-tellurite glasses," *J. Non. Cryst. Solids*, vol. 357, no. 1, pp. 88–95, 2011.

[52] T. Ozawa, "Kinetics of non-isothermal crystallization," *Polymer (Guildf).*, vol. 12, no. 3, pp. 150–158, 1971.

[53] H. E. Kissinger, "Variation of peak temperature with heating rate in differential thermal analysis," *J. Res. Natl. Bur. Stand. (1934).*, vol. 57, no. 4, p. 217, 1956.

[54] C. Dohare, "Investigation of Crystallization Kinetics in Glassy Se and Binary Se₉₈m₂ (M=Ag, Cd, Zn) Alloys Using DSC Technique in Non-Isothermal Mode," *J. Cryst. Process Technol.*, vol. 02, no. 04, pp. 139–146, 2012.

[55] Q. Wang, C. T. Liu, Y. Yang, J. B. Liu, Y. D. Dong, and J. Lu, "The atomic-scale mechanism for the enhanced glass-forming-ability of a Cu-Zr based bulk metallic glass with minor element additions.," *Sci. Rep.*, vol. 4, p. 4648, 2014.

[56] K. W. Park, J. Il Jang, M. Wakeda, Y. Shibutani, and J. C. Lee, "Atomic packing density and its influence on the properties of Cu-Zr amorphous alloys," *Scr. Mater.*,

vol. 57, pp. 805–808, 2007.

[57] X. D. Wang, S. Yin, Q. P. Cao, J. Z. Jiang, H. Franz, and Z. H. Jin, "Atomic structure of binary Cu64.5Zr35.5 bulk metallic glass," *Appl. Phys. Lett.*, vol. 92, no. 1, p. 011902, 2008.

[58] Z. D. Sha, Y. W. Zhang, Y. P. Feng, and Y. Li, "Molecular dynamics studies of short to medium range order in Cu64Zr36 metallic glass," *J. Alloys Compd.*, vol. 509, no. 33, pp. 8319–8322, 2011.

[59] Z. D. Sha, Y. P. Feng, and Y. Li, "Statistical composition-structure-property correlation and glass-forming ability based on the full icosahedra in Cu-Zr metallic glasses," *Appl. Phys. Lett.*, vol. 96, no. 6, 2010.

[60] H. W. Sheng, W. K. Luo, F. M. Alamgir, J. M. Bai, and E. Ma, "Atomic packing and short-to-medium-range order in metallic glasses.," *Nature*, vol. 439, no. 7075, pp. 419–425, 2006.

[61] Q. Wang, C. T. Liu, Y. Yang, Y. D. Dong, and J. Lu, "Atomic-scale structural evolution and stability of supercooled liquid of a Zr-based bulk metallic glass," *Phys. Rev. Lett.*, vol. 106, no. MAY, pp. 1–4, 2011.

[62] Y. Q. Cheng, H. W. Sheng, and E. Ma, "Relationship between structure, dynamics, and mechanical properties in metallic glass-forming alloys," *Phys. Rev. B - Condens. Matter Mater. Phys.*, vol. 78, no. 1, pp. 1–7, 2008.

[63] Y. Q. Cheng and E. Ma, "Indicators of internal structural states for metallic glasses: Local order, free volume, and configurational potential energy," *Appl. Phys. Lett.*, vol. 93, no. 5, pp. 8–11, 2008.

[64] G. a. Almyras, G. M. Matenoglou, P. Komninou, C. Kosmidis, P. Patsalas, and G. a. Evangelakis, "On the deposition mechanisms and the formation of glassy Cu-Zr thin films," *J. Appl. Phys.*, vol. 107, no. 2010, 2010.

[65] X. P. Nie, X. H. Yang, and J. Z. Jiang, "Ti microalloying effect on corrosion resistance and thermal stability of CuZr-based bulk metallic glasses," *J. Alloys Compd.*, vol. 481, no. 1–2, pp. 498–502, 2009.

Figures

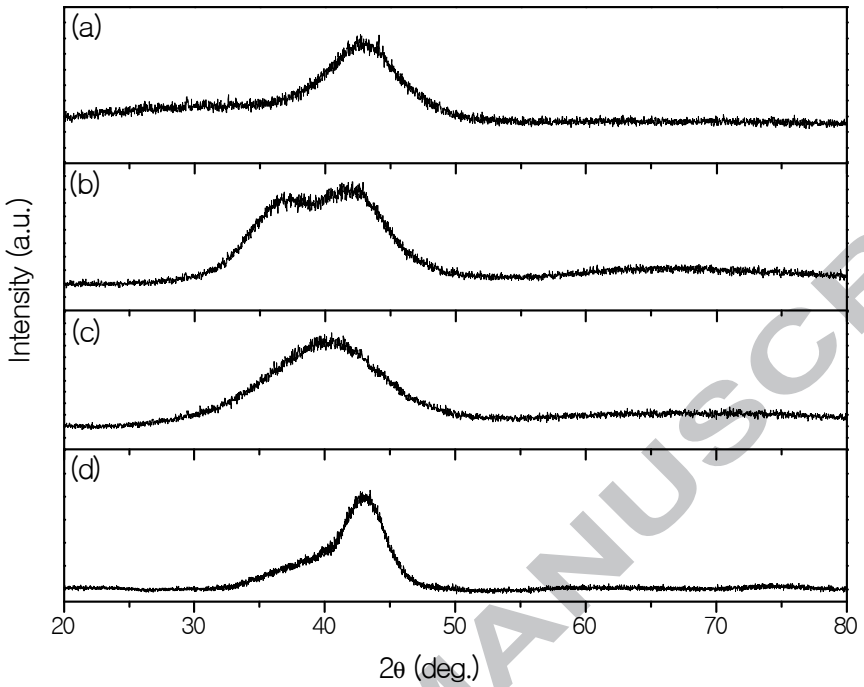

Figure 1: XRD pattern of (a) $Zr_{40.5}Ni_{59.5}$, (b) $Zr_{56.2}Cu_{43.8}$, (c) $Zr_{30}Cu_{57.7}Y_{12.3}$, and (d) $Zr_{32}Cu_{57.3}Ti_{10.7}$ alloys after fabrication by magnetron sputtering.

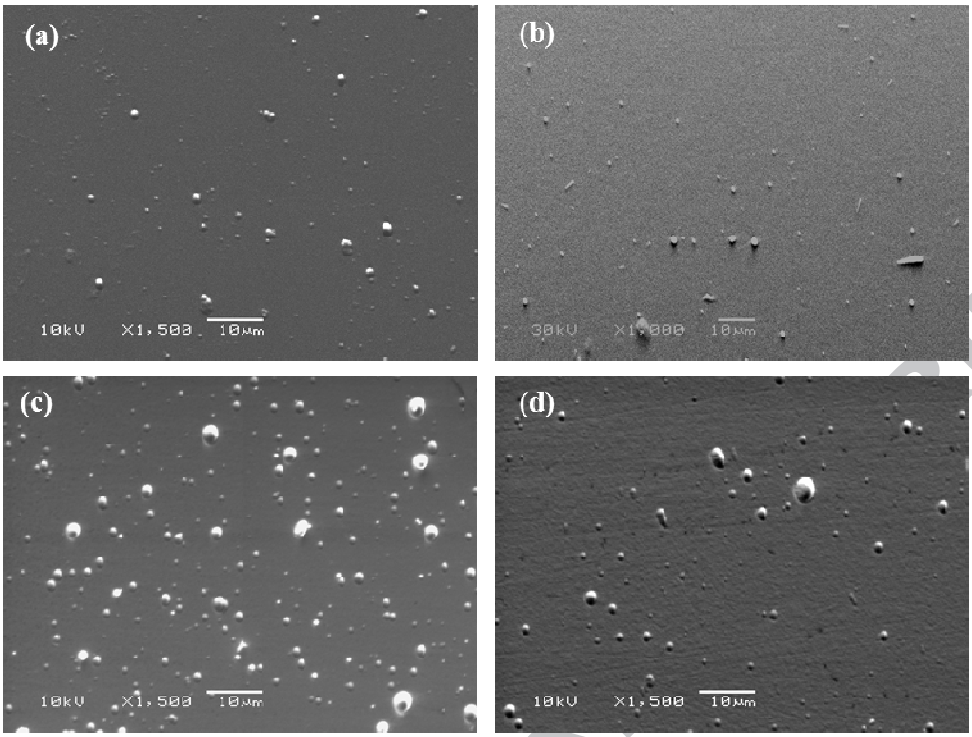

Figure 2: SEM images of the surface topography of the thin films (a) $Zr_{40.5}Ni_{59.5}$, (b) $Zr_{56.2}Cu_{43.8}$, (c) $Zr_{30}Cu_{57.7}Y_{12.3}$, and (d) $Zr_{32}Cu_{57.3}Ti_{10.7}$ after deposition.

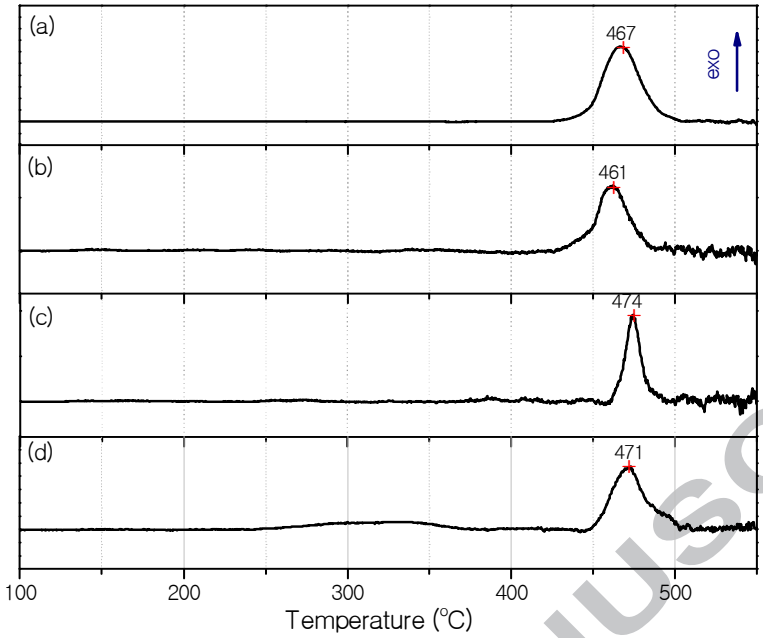

Figure 3: DSC thermograms showing the crystallisation temperature range of (a) $Zr_{40.5}Ni_{59.5}$, (b) $Zr_{56.2}Cu_{43.8}$, (c) $Zr_{30}Cu_{57.7}Y_{12.3}$, and (d) $Zr_{32}Cu_{57.3}Ti_{10.7}$ alloys under Ar with a heating rate of 5 °C min^{-1}.

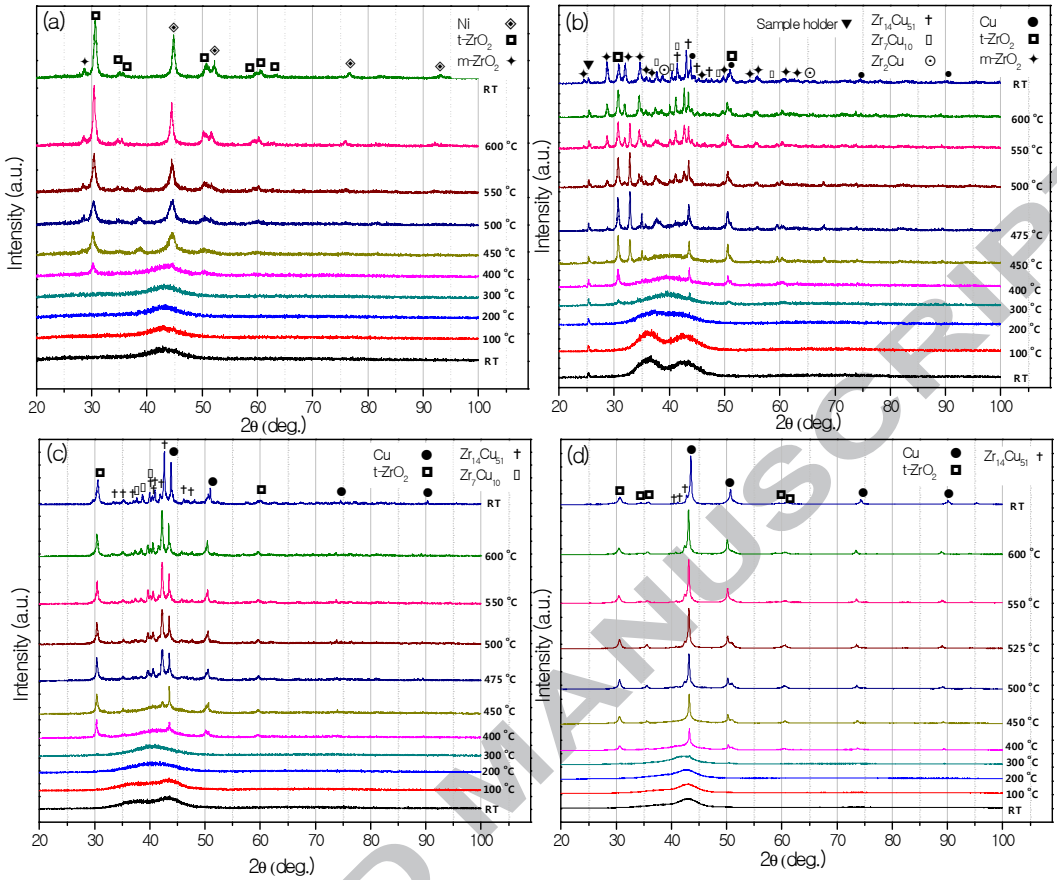

Figure 4: Evolution of *in-situ* XRD patterns for (a) $Zr_{40.5}Ni_{59.5}$, (b) $Zr_{56.2}Cu_{43.8}$, (c) $Zr_{30}Cu_{57.7}Y_{12.3}$, and (d) $Zr_{32}Cu_{57.3}Ti_{10.7}$ alloys as a function of temperature under 3 bar flowing He and a heating rate of 2 °C min^{-1}. The first and the last XRD patterns were collected at Room Temperature (RT).

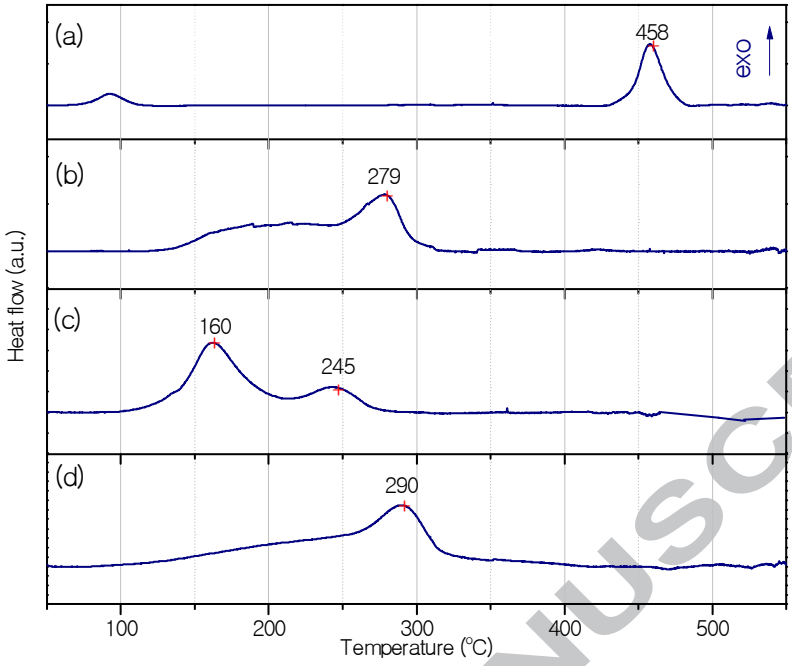

Fig 5: DSC thermograms showing the crystallisation temperature range of (a) $Zr_{40.5}Ni_{59.5}$, (b) $Zr_{56.2}Cu_{43.8}$, (c) $Zr_{30}Cu_{57.7}Y_{12.3}$, and (d) $Zr_{32}Cu_{57.3}Ti_{10.7}$ alloys under 3 bar hydrogen with a heating rate of 5 °C min^{-1}.

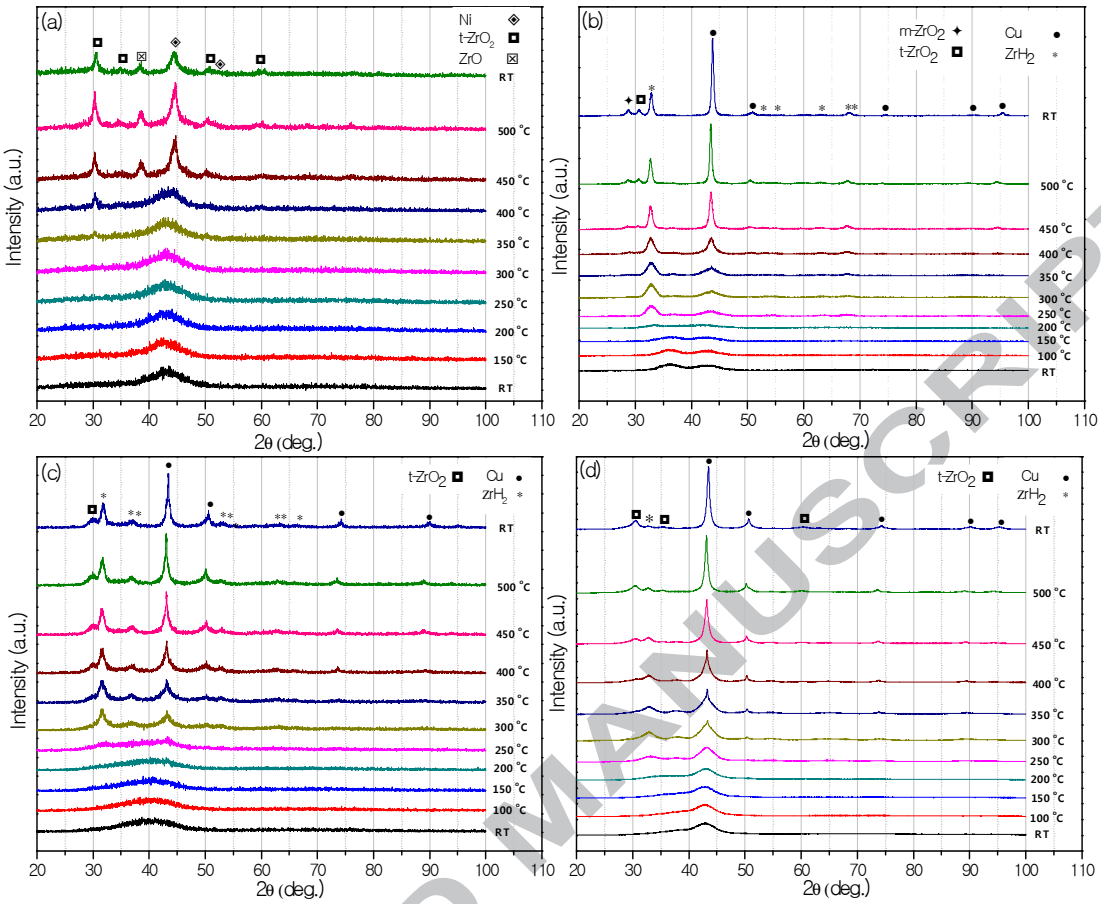

Figure 6: Evolution of *in-situ* XRD patterns for (a) $Zr_{40.5}Ni_{59.5}$, (b) $Zr_{56.2}Cu_{43.8}$, (c) $Zr_{30}Cu_{57.7}Y_{12.3}$, and (d) $Zr_{32}Cu_{57.3}Ti_{10.7}$ alloys as a function of temperature under 3 bar flowing hydrogen and a heating rate of 2 °C min^{-1}. The first and the last XRD patterns were collected at Room Temperature (RT).

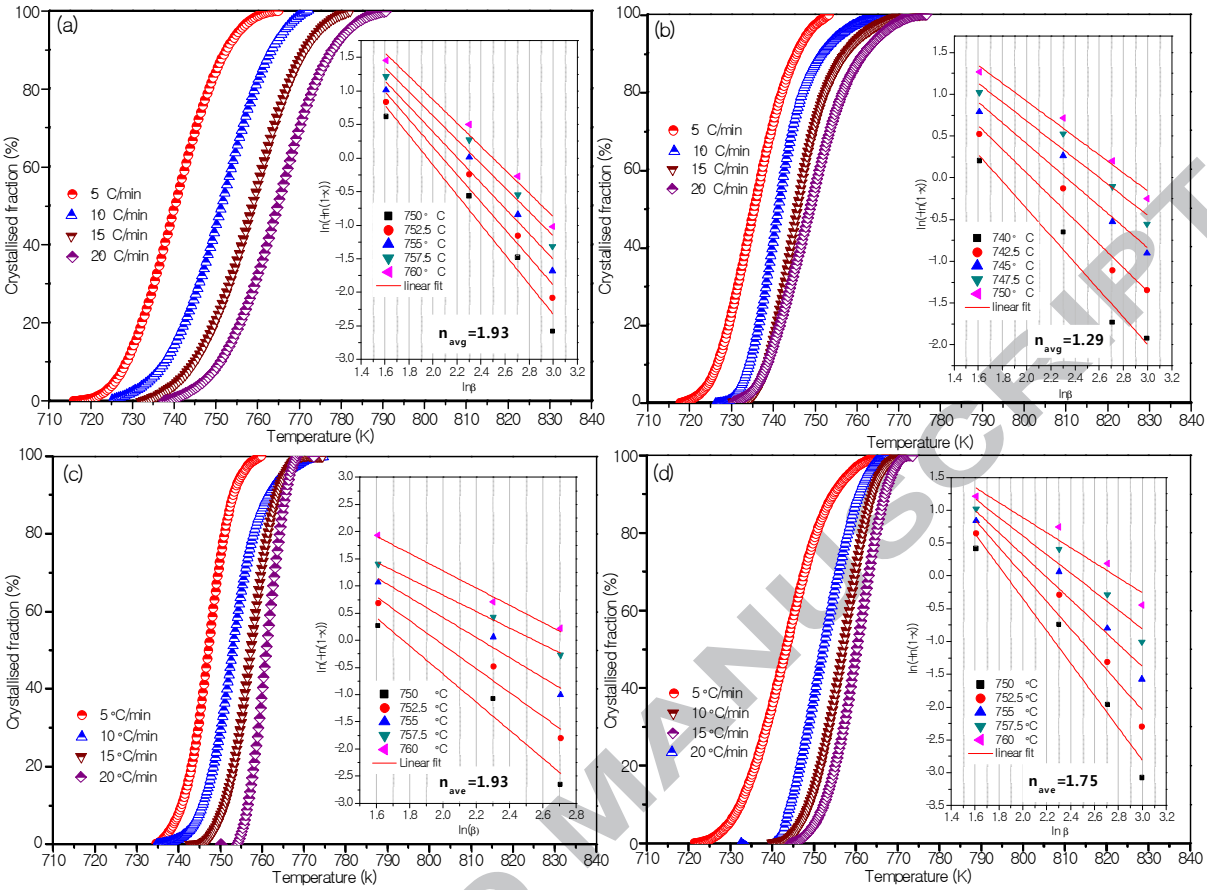

Figure 7: Crystallised fraction of (a) $Zr_{40.5}Ni_{59.5}$, (b) $Zr_{56.2}Cu_{43.8}$, (c) $Zr_{30}Cu_{57.7}Y_{12.3}$, and (d) $Zr_{32}Cu_{57.3}Ti_{10.7}$ alloys as a function of temperature at different heating rates. The inset graphs are plots of *ln[-ln(1-x)]* vs. *lnβ* at different temperatures to calculate the average Avrami exponent, *n*, according to the Ozawa method [52].

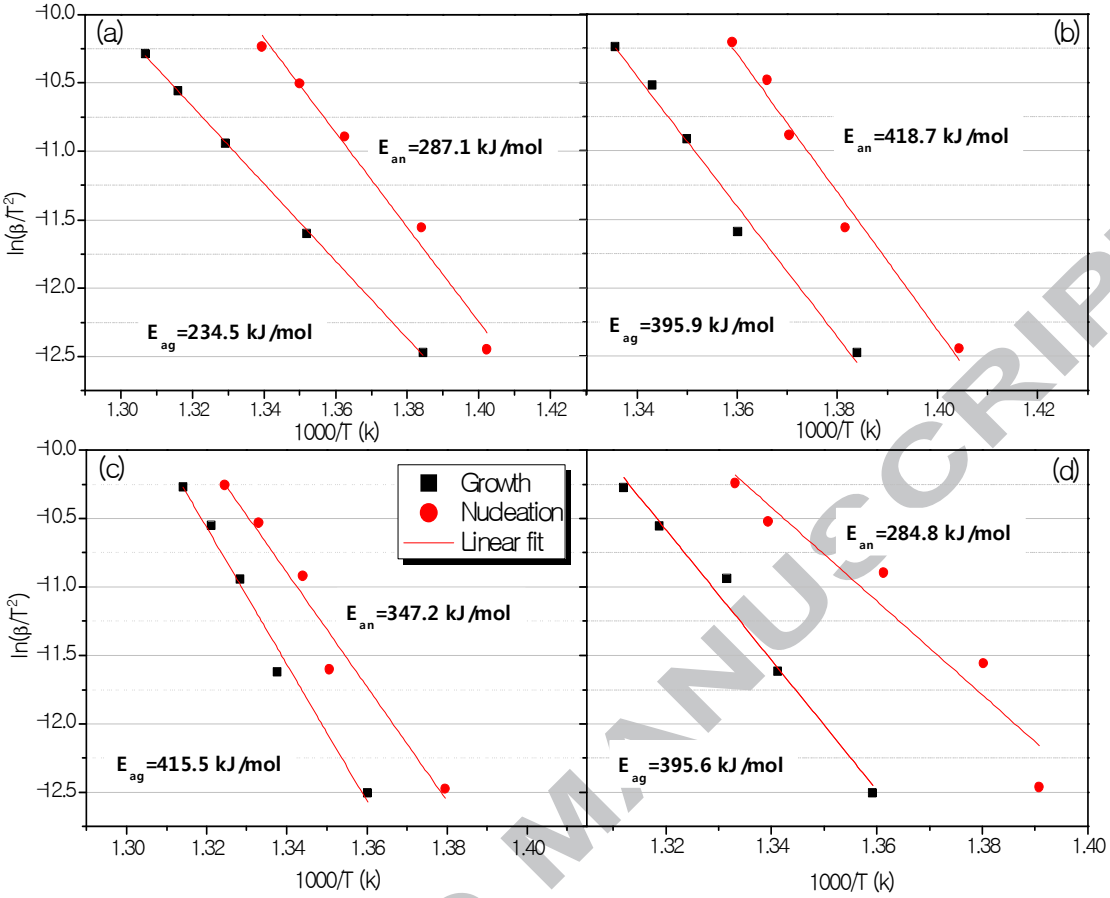

Figure 8: Activation energies for nucleation (●) and growth (■) processes of (a) $Zr_{40.5}Ni_{59.5}$, (b) $Zr_{56.2}Cu_{43.8}$, (c) $Zr_{30}Cu_{57.7}Y_{12.3}$, and (d) $Zr_{32}Cu_{57.3}Ti_{10.7}$ alloys calculated by the Kissinger method [53] with heating rates of 2, 5, 10, 15 and 20 °C min^{-1}.

Tables

Table 1: Sputtering conditions and EDS analyses of the fabricated thin films. The film thicknesses and the activation energies for nucleation and growth (see Fig. 5) of each sample are also listed.

Alloy	Target current (A)				EDS (at.%)	Film thickness (μm)	E_a (kJ/mol)		Avrami exponent (n)
	Zr	Cu	Y	Ni			Nucleation	Growth	
$Zr_{36}Ni_{64}$	0.76	-	-	0.5	$Zr_{40.5}Ni_{59.5}$	3.5	287.1±2.4	234.5±0.6	1.93
$Zr_{54}Cu_{46}$	1.42	0.5	-	-	$Zr_{56.2}Cu_{43.8}$	5.7	418.7±1.8	395.9±1.7	1.29
$Zr_{30}Cu_{60}Y_{10}$	1.25	0.8	0.5	-	$Zr_{30}Cu_{57.7}Y_{12.3}$	5.9	347.2±3	415.5±1.6	1.93
$Zr_{30}Cu_{60}T_{10}$	1.23	0.8	0.5	-	$Zr_{32}Cu_{57.3}Ti_{10.7}$	8.3	395.6±5.6	284.8±1.7	1.75

Table 2: Crystal structure refinement results for $Zr_{40.5}Ni_{59.5}$, $Zr_{56.2}Cu_{43.8}$, $Zr_{30}Cu_{57.7}Y_{12.3}$, and $Zr_{32}Cu_{57.3}Ti_{10.7}$ alloys heat treated at 500 and 650 °C under 3 bar Ar for 2h.

Alloy	Phases		Abundance (wt. %)	Structure	Lattice parameters (Å)
	500 °C	650 °C			
$Zr_{40.5}Ni_{59.5}$	Ni		66	c	a=b=c= 3.512
	ZrO_2		24	t	a=b= 3.592, c= 5.183
	ZrO_2		9	m	a=5.234, b= 5.001, c=5.794
	ZrO		1	c	a=b=c= 4.034
		Ni	41	c	a=b=c= 3.523
		ZrO_2	21	t	a=b= 3.591, c= 5.174
		ZrO_2	38	m	a= 4.937, b= 5.306, c= 5.352
$Zr_{56.2}Cu_{43.8}$	Cu		15	c	a=b=c= 3.617
	ZrO_2		8	t	a=b= 3.607, c= 5.168
	ZrO_2		15	m	a=5.125, b= 5.204, c=5.328
	Zr_7Cu_{10}		62	o	a=9.348, b=9.318, c=12.619
		Cu	8	c	a=b=c= 3.613
		ZrO_2	8	t	a=b= 3.593, c= 5.165
		Zr_7Cu_{10}	46	o	a=9.326, b=9.300, c=12.604
		$Zr_{14}Cu_{51}$	31	h	a=b= 11.213, c= 8.250
		Zr_2Cu	7	c	a=b=c= 12.235
$Zr_{30}Cu_{57.7}Y_{12.3}$	Cu		14	c	a=b=c= 3.616
	ZrO_2		27	t	a=b= 3.638, c= 5.158
	$Zr_{14}Cu_{51}$		49	h	a=b= 11.352, c= 8.378
	Zr_7Cu_{10}		10	o	a=9.449, b=9.403, c=12.344
		ZrO_2	8	t	a=b= 3.737, c= 5.052
		$Zr_{14}Cu_{51}$	87	h	a=b= 11.343, c= 8.364
		Zr_7Cu_{10}	5	o	a=9.422, b=9.433, c=12.406
$Zr_{32}Cu_{57.3}Ti_{10.7}$	Cu		18	c	a=b=c= 3.614
	ZrO_2		10	t	a=b= 3.556, c= 5.081
	$Zr_{14}Cu_{51}$		72	h	a=b= 11.236, c= 8.226
		ZrO_2	2	t	a=b= 3.629, c= 5.083
		$Zr_{14}Cu_{51}$	98	h	a=b= 11.254, c= 8.270

Highlights

1- Amorphous Zr-based thin films fabricated by the magnetron sputtering method.

2- Hydrogen significantly reduces the thermal stability of amorphous alloys.

3- Decomposition of amorphous phase leads to phase separation during crystallisation.

4- Phase separation seems to change the crystallisation path and products.